Sensors and Materials, Vol. 38, No. 2 (2026) 663–672
MYU Tokyo

S & M 4335

Synthesis and Photoluminescence Characterization of Eu-doped $Tb_3Al_{5-x}Ga_xO_{12}$ Nanoparticle Scintillators via Sol–Gel Method for Biological Applications

Yuma Takahashi,[1] Hiroki Kawamoto,[2] Yutaka Fujimoto,[2]
Keisuke Asai,[2] and Masanori Koshimizu[1*]

[1]Department of Electronics and Materials Science, Shizuoka University,
3-5-1 Johoku, Chuo-ku, Hamamatsu 432-8011, Japan
[2]Department of Applied Chemistry, Tohoku University, 6-6-07 Aoba, Aramaki, Aoba-ku, Sendai 980-8579, Japan

(Received October 31, 2025; accepted December 15, 2025)

Keywords: scintillator, nanoparticle, TAGG, garnet, phosphor

Red-emitting Eu-doped $Tb_3Al_xGa_{5-x}O_{12}$ (TAGG) nanoparticles were synthesized via a sol–gel method to develop scintillators applicable to *in vivo* use. The nanoparticles had diameters of approximately 100–200 nm. X-ray diffraction patterns indicate that the samples possessed a garnet structure. Photoluminescence (PL) spectra exhibited an emission peak mainly at 589 nm, corresponding to the $^5D_0 \rightarrow {}^7F_1$ transitions of Eu^{3+} ions. PL quantum yield reached over 90% at the maximum. Upon X-ray irradiation, all the samples exhibited red emission. These results indicate that the developed nanoparticles are applicable as biocompatible scintillators for *in vivo* applications, exhibiting scintillation in the red wavelength region mainly at 592 and 709 nm.

1. Introduction

Luminescent materials used for radiation detection are generally classified into two categories in accordance with their emission behaviors: scintillators that exhibit prompt luminescence and storage phosphors that temporarily store absorbed radiation energy.[1–3] Scintillators emit light immediately after irradiation and are widely employed in fields that require real-time detection, such as medical imaging systems and radiation monitoring.[4–9] In contrast, storage phosphors trap radiation-induced electrons and holes at trap energy levels, and the carriers subsequently recombine under optical or thermal stimulation to produce luminescence.[10–13] This luminescence property enables the evaluation of radiation dose and the visualization of its distribution, and such materials are used in imaging plates and dosimeters.[14–17] Recently, materials exhibiting both scintillation and storage luminescence have also been reported.[18,19]

Scintillators are phosphor materials that emit photons upon interaction with ionizing radiation. They are widely utilized as sensors for the detection of ionizing radiation in combination with photon detectors such as photomultiplier tubes and photodiodes. Scintillators

*Corresponding author: e-mail: koshimizu.masanori@shizuoka.ac.jp
https://doi.org/10.18494/SAM6070

ISSN 0914-4935
https://myukk.org/

can generally be classified into inorganic[20–22] and organic[23–25] ones. Inorganic scintillators typically exhibit high light yields and high interaction probabilities with high-energy photons such as X-rays and γ-rays, whereas organic scintillators usually have lower light yields but provide faster scintillation rise and decay. Depending on the purpose of use, appropriate scintillators are selectively used, and they play important roles in medical, environmental, and fundamental physics research.

There is currently a growing demand for technologies that can induce scintillation *in vivo* for medical and biological research. Recently, the successful control of mouse behavior through external X-ray irradiation using Ce-doped $Ga_3Al_{5-y}Ga_yO_{12}$ (GAGG:Ce) nanoparticle scintillators coupled with neurons and photoreceptor molecules has been achieved.[26] For *in vivo* applications of scintillators, several requirements must be satisfied: high light yield for efficient emission, high interaction probability with X-rays to enable excitation from outside the body, and chemical stability to ensure structure integrity and biocompatibility under physiological conditions. Furthermore, miniaturization into nanoparticles is important to minimize invasiveness during introduction into biological bodies. In one report,[26] the neuronal activation efficiency was approximately 45% when using nanoparticles, whereas it was only around 10% with microparticles, indicating that size miniaturization directly contributes to improved responsiveness. Therefore, controlling the particle size is one of the critical design factors for *in vivo* applications. Ce-doped GAGG nanoparticle scintillators, which exhibit high light yield and chemical stability,[26] have therefore been considered suitable for *in vivo* use. On the other hand, among materials with a garnet structure, Tb-based garnet materials such as $Tb_3Ga_5O_{12}$ (TGG), $Tb_3Al_5O_{12}$ (TAG), and their solid solution $Tb_3Al_xGa_{5-x}O_{12}$ (TAGG) are also known as luminescent materials exhibiting green emission originating from the $^5D_4 \rightarrow {}^7F_j$ transitions of Tb^{3+} ions, and it has been reported that the incorporation of other activator ions, such as Ce^{3+} and Er^{3+}, results in characteristic emissions corresponding to the dopant ions.[27–29] In addition, in TAGG, variations in the Al/Ga ratio have been reported to alter the crystal field strength and local symmetry, leading to changes in the luminescence properties.[30] Owing to these features, TAGG can accommodate various rare-earth activator ions and is considered suitable for the development of scintillators and phosphors.

In this study, we aimed to develop red-emitting nanoparticle scintillators applicable to photoreceptor molecules with absorption bands in the red wavelength region. Eu-doped TAGG nanoparticles were synthesized via the sol–gel method. TAGG was selected as the host material because it possesses a garnet structure analogous to that of GAGG and exhibits high chemical stability as well as a high interaction probability with X-rays. Eu^{3+} ions were chosen as the luminescent centers to obtain red emission and to take advantage of possible energy transfer from Tb^{3+} to Eu^{3+}.[31] In powder scintillators, the scintillation is often scattered and absorbed among particles, and the quantitative estimation of scintillation light yield based on the pulse height spectra is difficult. Therefore, we investigated the synthesis conditions to obtain a high internal photoluminescence (PL) quantum yield (QY). The light output L can be described as

$$L = \frac{10^6}{2.3E_g}\beta SQ, \tag{1}$$

where E_g, β, S, and Q represent the bandgap energy of the host material, energy efficiency of the conversion to electron–hole pairs, energy-transfer efficiency from the host to the luminescence centers, and PL QY, respectively.[32] The scintillation light yield is proportional to the PL QY. Hence, we optimized the compositions for the PL QY.

2. Materials and Methods

The host composition $Tb_3Al_xGa_{5-x}O_{12}$ was adopted. $Tb(NO_3)_3{\cdot}5H_2O$ (99.9%, Sigma-Aldrich), $Al(NO_3)_3{\cdot}9H_2O$ (99.997%, Sigma-Aldrich), $Ga(NO_3)_3{\cdot}nH_2O$ (99.999%, Kojundo Chemical), $Eu(NO_3)_3{\cdot}6H_2O$ (99.9%, Sigma-Aldrich), $C_4H_6O_6$ (tartaric acid, 99.5%, Fujifilm Wako), and distilled water (Fujifilm Wako) were used without further purification.

The sol–gel method was employed for synthesis. The nitrates of Tb, Al, and Ga were dissolved in 25 mL of a 0.6 mol/L aqueous solution of tartaric acid in accordance with the stoichiometric ratio. Additionally, Eu nitrate was dissolved at a concentration of 0.01–15 mol% with respect to the cations in the Tb sites. The total nitrate amount was half the molar amount of tartaric acid. The solution was stirred for 24 h under a closed lid and then heated at 80 ℃ for 2 h. Subsequently, the lid was removed, and the solution was heated at 80 ℃ to obtain a dry gel. The resulting dry gel was subsequently ground in a mortar and calcined in an electric furnace at 1300 ℃ for 6 h to yield the final samples.

To achieve high PL QY, the host composition was optimized at a fixed Eu concentration of 0.75 mol%. Samples with x = 0, 1, 2, 3, 4, and 5 were prepared. As will be discussed in Results and Discussion, the sample with x = 0 exhibited the highest PL QY. On the basis of the result, the Eu concentration was optimized with the host composition with x = 0. Samples were prepared with Eu doping concentrations of 0.01, 0.03, 0.1, 0.3, 0.75, 0.1, 5, 10, and 15 mol%.

The X-ray diffraction (XRD) patterns were measured using an X-ray diffractometer (RINT2200, Rigaku). The transmission electron microscopy (TEM) images were obtained using a scanning transmission electron microscope (STEM; JEM-2100, JEOL). The PL and excitation spectra were measured using a fluorescent spectrometer (RF-5300PC, Shimadzu). The PL decay profiles were measured using a spectrofluorometer by the time-correlated single photon counting technique (Delta Flex 3000U-TMK2, Horiba). The PL QY was evaluated using an absolute PL quantum yield spectrofluorometer (C11347, Hamamatsu). The X-ray-induced luminescence (XRL) spectra were obtained under X-ray irradiation (XRB80N100, Spellman). The scintillation from the samples was detected with a CCD detector (Shamrock 163 Spectrograph combined with Newton 920, Andor).

3. Results and Discussion

Figure 1 shows (a) the XRD patterns of the TAGG:0.75% Eu (x = 0) sample (top) compared with the reference patterns of TGG and monoclinic β-Ga_2O_3, (b) the XRD patterns of TAGG:0.75%Eu (x = 0–5), and (c) the XRD patterns of TGG:0.01–15% Eu. The XRD pattern of TGG:0.75%Eu^{3+} closely matched that in the database of the $Tb_3Ga_5O_{12}$ phase (JCPDS file No. 01-088-0575). As shown in Fig. 1(a), small peaks corresponding to β-Ga_2O_3 were also observed

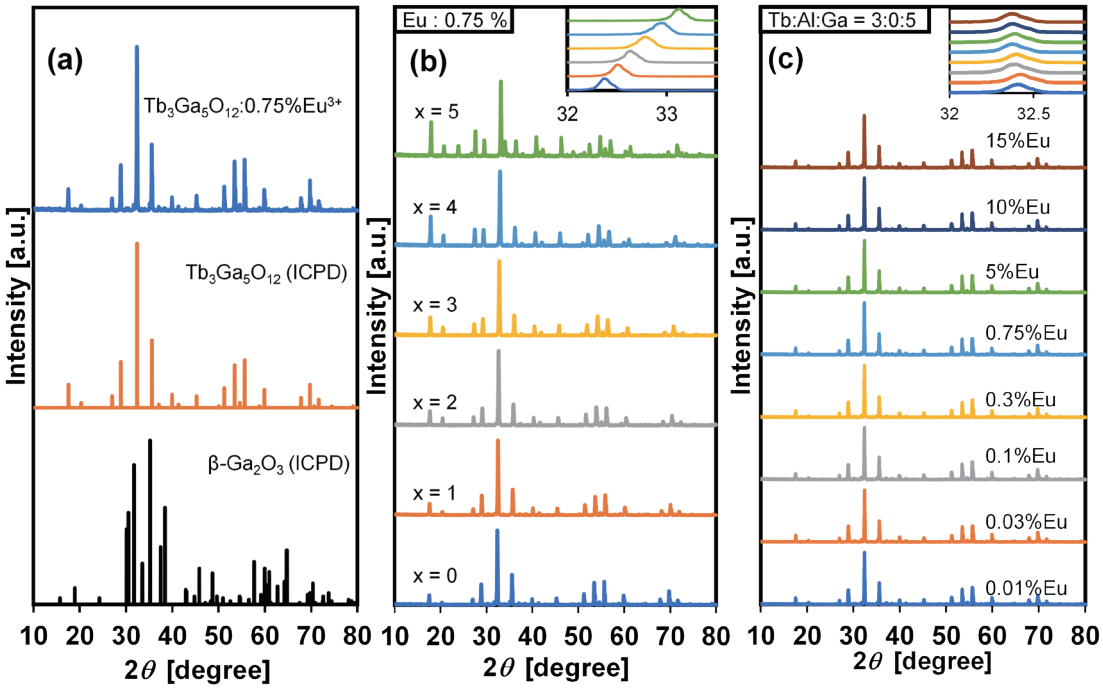

Fig. 1. (Color online) (a) XRD patterns of TGG:0.75% Eu^{3+} sample (top) compared with reference patterns of TGG (#01-088-0575) and monoclinic β-Ga_2O_3 (#01-087-1901). (b) XRD patterns of TAGG:0.75%Eu (x = 0–5). Inset: enlarged view of (420) diffraction peak region. (c) XRD patterns of TGG:0.01–15% Eu.

at 31.6°, indicating the presence of a small amount of β-Ga_2O_3. In Fig. 1(b), all samples with (x = 0–4) exhibited diffraction peaks corresponding to the TAGG phase. For the Ga-rich composition (x = 5), an additional small diffraction peak at 2θ = 23.6° corresponding to α-Ga_2O_3 was observed, suggesting the appearance of the minor secondary phase of α-Ga_2O_3.[33] As shown in the inset of Fig. 1(b), a significant shift of the (420) diffraction peak to the higher angle side was observed, which is due to the incorporation of Al^{3+} ions (0.535 Å)[34] at the Ga^{3+} site, which has a larger ionic radius (0.620 Å).[34] Meanwhile, as shown in Fig. 1(c), a slight shift of the diffraction peaks toward lower angles was observed with increasing Eu concentration, which is due to the incorporation of Eu^{3+} ions (1.066 Å)[34] at the Tb^{3+} site, which has a smaller ionic radius (1.04 Å).[34]

Figure 2 shows the TEM image of TGG:0.75% Eu. The observed particles were predominantly elliptical in shape, with some round and angular ones also observed. The particle size ranged from approximately 100 to 200 nm. A similar particle morphology was observed for all the samples. The morphology and particle size of the nanoparticles are comparable to those of Eu- and Ce-doped GAGG nanoparticles.[35,36]

Figure 3 shows the PL and PLE spectra of TGG:0.75% Eu. In the PL spectra, we observed peaks at 589, 608, 647, and 691 nm for samples with x values ranging from 0 to 5. According to a previous report on TGG:Eu^{3+}, these peaks are attributed to the $^5D_0 \rightarrow {}^7F_1$, $^5D_0 \rightarrow {}^7F_2$, $^5D_0 \rightarrow {}^7F_3$, and $^5D_0 \rightarrow {}^7F_4$ electronic transitions of Eu^{3+}, respectively.[37–39] In the PLE spectra, we observed a

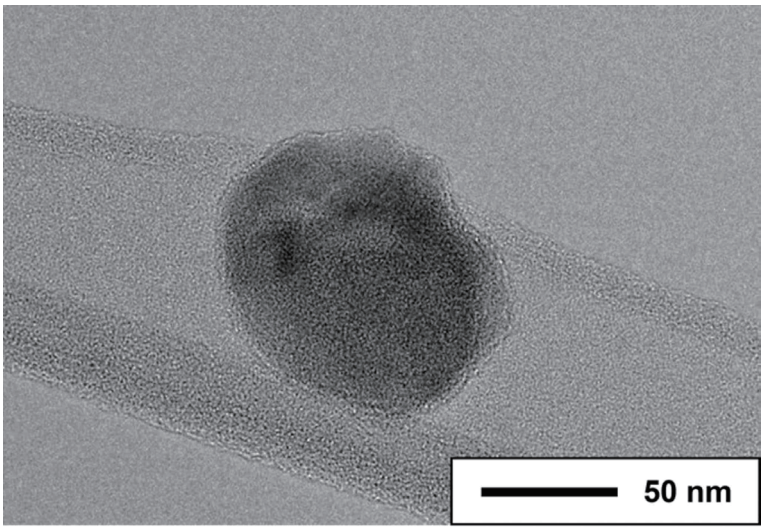

Fig. 2. TEM image of TGG: 0.75%Eu nanoparticle.

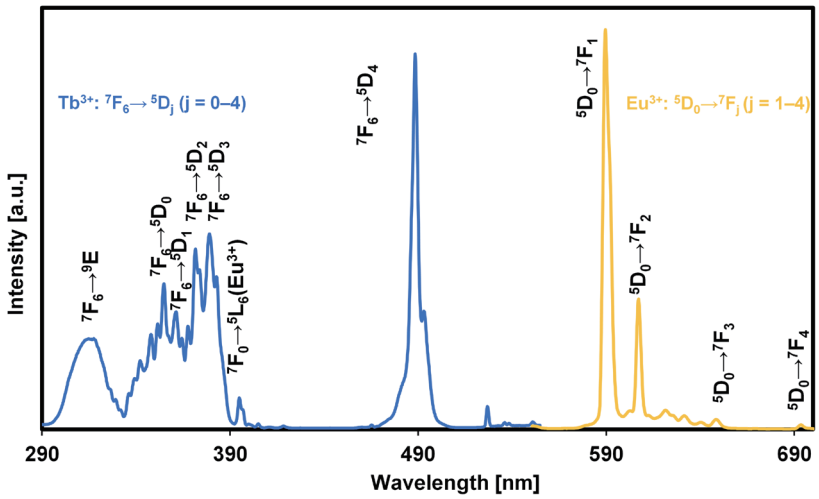

Fig. 3. (Color online) Room-temperature PL and PLE spectra of TGG:0.75%Eu sample measured with λ_{ex} = 350 nm and λ_{em} = 590 nm, respectively.

broad peak at around 316 nm and sharp peaks at 355, 361, 371, 379, and 488 nm. According to previous reports, the broad peak is attributable to the $^7F_6 \rightarrow {}^9E$ transition of Tb^{3+}, and the sharp peaks to the $^7F_6 \rightarrow {}^5D_0$, $^7F_6 \rightarrow {}^5D_1$, $^7F_6 \rightarrow {}^5D_2$, $^7F_6 \rightarrow {}^5D_3$, and $^7F_6 \rightarrow {}^5D_4$ transitions of Tb^{3+}.[40,41] In addition, a peak at approximately 395 nm, assigned to the $^7F_0 \rightarrow {}^5L_6$ transition of Eu^{3+}, was also observed.[38]

Figure 4 shows the PL and PLE spectra of TAGG:0.75% Eu samples with different Al/Ga ratios (x = 0–5). The emission peaks at 592 nm, corresponding to the $^5D_0 \rightarrow {}^7F_1$ transitions of Eu^{3+}, exhibit a clear tendency to split with increasing x. This peak splitting can be attributed to the Stark effect in the 4f–4f transitions of Eu^{3+} ions. It is well known that the $^5D_0 \rightarrow {}^7F_j$ (J = 1, 2, …) transitions of Eu^{3+} split into multiple Stark components owing to the crystal-field-

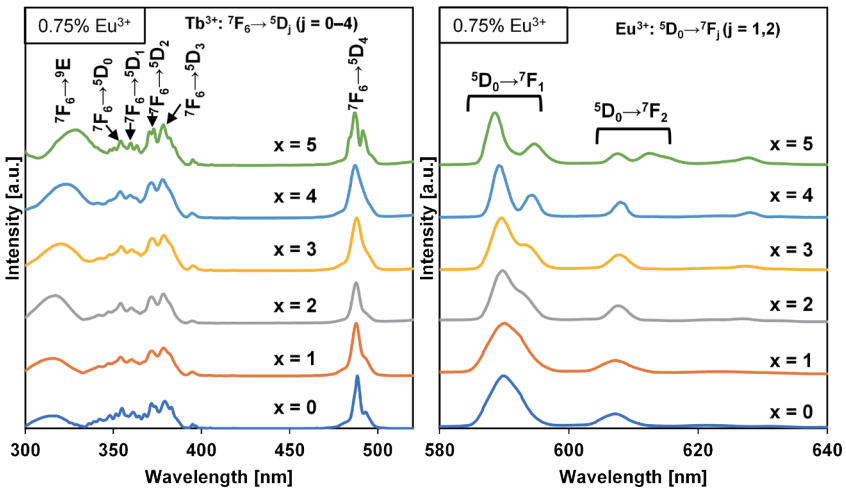

Fig. 4. (Color online) (a) Room-temperature PLE spectra of TAGG:0.75%Eu (x = 0–5) sample measured with λ_{em} = 590 nm, and (b) room-temperature PL spectra of TAGG:0.75%Eu (x = 0–5) sample measured with λ_{ex} = 350 nm.

induced splitting of the ^7F_j levels.[39] In the present system, the substitution of smaller Al^{3+} ions (0.535 Å)[34] for larger Ga^{3+} ions (0.62 Å)[34] results in lattice contraction, reduced local symmetry around Eu^{3+} ions, and an enhancement of the crystal field strength. Consequently, the energy separation between the ^7F_j sublevels becomes larger, and emission lines that were previously overlapped become distinguishable.[42]

Figure 5 shows the PLE and PL spectra of TGG:0.01–15% Eu. In the PLE spectra (a), a peak attributed to the $^7F_0 \rightarrow {}^5L_6$ transition of Eu^{3+} appears at approximately 395 nm[36] for Eu concentrations above 0.3%, and its intensity increases with increasing Eu content. In the PL spectra (b), the emission corresponding to the $^5D_4 \rightarrow {}^7F_5$ transition of Tb^{3+} (~543 nm)[39] is observed at low Eu concentrations (0.01–0.1 %), and its intensity decreases as the Eu concentration increases. The decrease in Tb^{3+}-related emission intensity with increasing Eu^{3+} concentration suggests the energy transfer from Tb^{3+} to Eu^{3+}. Figure 6 shows the PL decay curves measured at λ_{em} = 550 nm ($^5D_4 \rightarrow {}^7F_5$ transition of Tb^{3+}) in the TGG:0.01–15% Eu samples under λ_{ex} = 267 nm ($4f^8 \rightarrow 4f^7 5d^1$ excitation of Tb^{3+}). The decay behavior was well fitted using sums of three exponential functions, and the decay time constants and relative intensities obtained from the fitting are summarized in Table 1. In the Eu-doped samples, the first component (τ_1: 2–4 μs) is attributed to energy transfer from Tb^{3+} to closely located Eu^{3+}.[43] In the undoped sample, the contribution of the first component was as small as 1.3%. With increasing Eu concentration, this contribution sharply increased, reaching approximately 45% at Eu concentrations equal to or higher than 0.75 mol%. This suggests that the increase in Eu concentration promotes fast energy transfer in closely associated Tb^{3+}–Eu^{3+} pairs. The second component (τ_2: 20–40 μs) is considered to correspond to energy transfer between more distant Tb^{3+}–Eu^{3+} pairs.[44] As the Eu concentration increased, the contribution of the first component increased, whereas that of the second decreased from 58 to 30%, indicating that the energy-transfer pathway through closely associated pairs became dominant. The third component

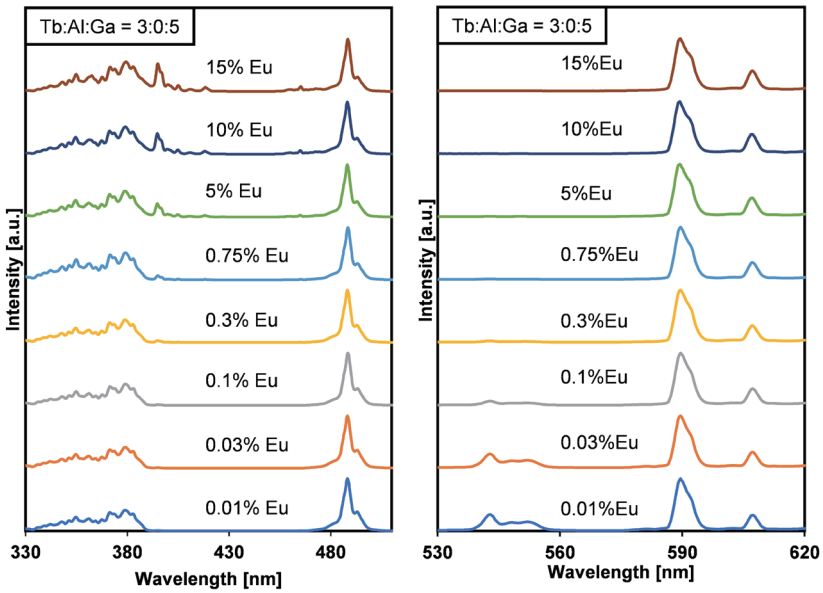

(a) (b)

Fig. 5. (Color online) (a) Room-temperature PLE spectra of TAGG:0.01–15% Eu sample measured with λ_{em} = 590 nm, and (b) room-temperature PL spectra of TGG:0.01–15% Eu sample measured with λ_{ex} = 350 nm.

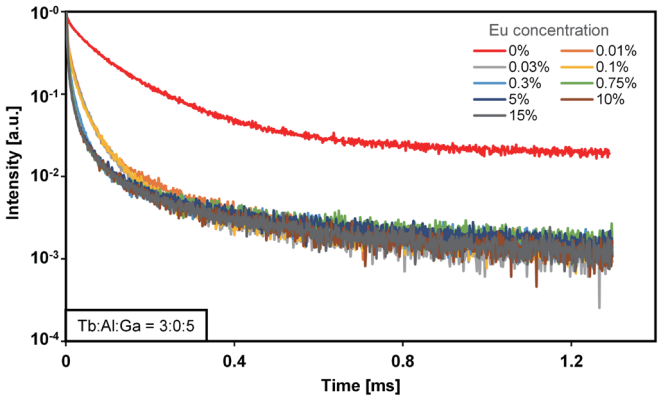

Fig. 6. (Color online) PL decay curves measured at λ_{em} = 550 nm (Tb^{3+} emission) in the TGG:0.01–15% Eu samples with λ_{ex} = 267 nm (Tb^{3+} excitation).

Table 1
Decay time constants (τ) and relative intensities (I) of each decay component obtained from the PL decay curves of TGG:0–15% Eu samples.

Eu concentration (%)	τ_1 (μs)	I_1 (%)	τ_2 (μs)	I_2 (%)	τ_3 (μs)	I_3 (%)
0	4.59	1.3	49.0	28.0	159	70.7
0.01	2.51	10.3	21.1	58.2	129	31.5
0.03	4.24	23.8	31.9	57.7	201	18.5
0.10	4.43	26.6	31.2	51.7	154	21.6
0.30	2.38	20.0	16.5	50.8	130	29.2
0.75	4.22	45.1	33.2	29.2	304	25.7
5	3.96	44.1	42.3	29.9	332	26.0
10	4.00	44.7	42.8	30.1	358	25.1
15	3.96	45.0	42.5	29.9	347	25.1

(τ_3: 130–350 μs) is considered to originate from delayed luminescence caused by electrons trapped at lattice defects or impurity-related levels, that is, a persistent-luminescence-related process. The relative contribution of this component decreased from 70 to 25% with increasing Eu concentration, suggesting that the enhancement of the energy transfer from Tb^{3+} to Eu^{3+} suppresses the trap-related emission.

Table 2 shows (a) the relationship between the Al/Ga ratio (x) and the PL QY of the sample with TAGG:0.75% Eu and (b) the relationship between the Eu concentration and the PL QY of the sample with $x = 0$. For the PL QY evaluation, the emission intensity integrated at 291–889 nm was used. The PL QY decreased with increasing x, and the highest PL QY (69%) was obtained at $x = 0$. This decrease is attributed to a change in the local coordination environment around Eu^{3+}, which reduces the intensity of the $^5D_0 \rightarrow {}^7F_1$ transition.[30] On the basis of these results, the Eu concentration was optimized for the $x = 0$ composition, which exhibited the highest PL QY. The PL QY increased with increasing Eu concentration, reaching a maximum (>90%) at 5% Eu. At higher Eu concentrations (>5%), however, the PL QY decreased owing to concentration quenching.

Figure 7 shows the XRL spectra of TAGG:0.75% Eu (x = 0–5) samples (a) and the TAGG:0.01–15% Eu sample (b) with undoped TGG. The emission peaks corresponding to the $^5D_0 \rightarrow {}^7F_1$ and $^5D_0 \rightarrow {}^7F_4$ transitions of Eu^{3+}[37–39] were observed at 592 and 709 nm, respectively, indicating the realization of red emission. As shown in Fig. 7(a), similar to the PL spectra, the splitting of the emission peaks associated with the $^5D_0 \rightarrow {}^7F_j$ transitions was observed with increasing x, which is attributed to the Stark effect in the 4f–4f transitions of Eu^{3+}ions.[39] In addition, in the scintillation spectra of the $x = 0$ sample, two emission peaks were observed at 612 and 615 nm. The 612 nm peak originates from the $^5D_0 \rightarrow {}^7F_2$ transition of Eu^{3+} ions occupying Tb^{3+} sites in the TAGG host, whereas the 615 nm peak is assigned to the same transition from Eu^{3+} ions incorporated in a minor α-Ga_2O_3 phase.[45]

Table 2
(a) PL QY of TAGG:0.75% Eu (x = 0–5) samples measured with λ_{ex} = 380 nm. (b) PL QY of TGG:0.01–15% Eu samples measured with λ_{ex} = 380 nm.

(a)

x	PL QY (%)
0	69.4
1	66.5
2	24.5
3	68.5
4	52.8
5	37.1

(b)

Eu concentration (%)	PL QY (%)
0.01	11.7
0.03	21.5
0.1	39.6
0.75	69.4
5	94.4
10	82.3
15	86.2

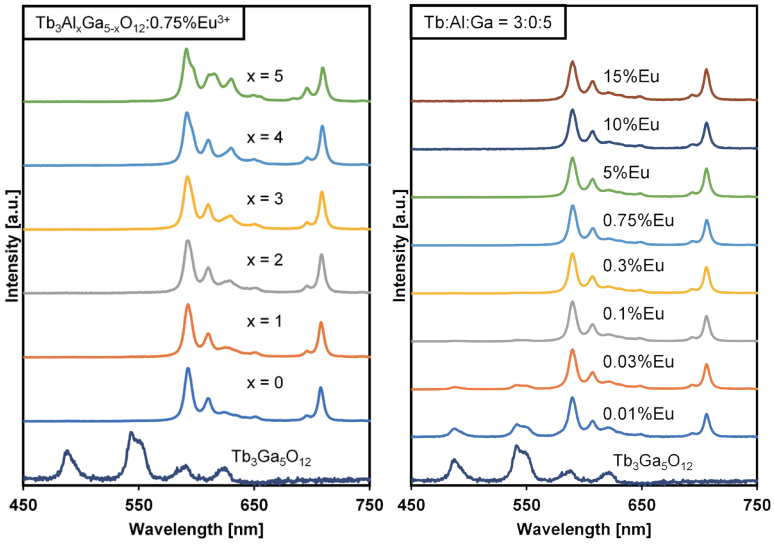

(a) (b)

Fig. 7. (Color online) (a) XRL spectra of TAGG:0.75% Eu (x = 0–5) sample and (b) TGG:0.01–15% Eu sample with undoped TGG.

4. Conclusions

Eu-doped TAGG nanoparticles were synthesized via the sol–gel method. The XRD patterns indicate the formation of the garnet phase. The TEM observations revealed that the particle size was approximately 100–200 nm. The PL spectra exhibited the emission peak mainly at 589 nm, corresponding to the $^5D_0 \rightarrow {}^7F_1$ transitions of Eu^{3+}, whereas the PL excitation (PLE) spectra showed excitation peaks mainly corresponding to the 4f–4f and 4f–5d transitions of Tb^{3+}. PL decay measurements suggested energy transfer from Tb^{3+} to Eu^{3+} during the luminescence process. The highest photoluminescence quantum yield was over 90% for TAGG: 5% Eu (x = 0). Upon X-ray irradiation, all the samples exhibited red emission at 592 and 709 nm, which are attributed to the $^5D_0 \rightarrow {}^7F_1$ and $^5D_0 \rightarrow {}^7F_4$ transitions of Eu^{3+}. These results reveal that TAGG:5% Eu (x = 0) is a promising material for biological applications that require bright scintillation under X-ray irradiation, owing to its small particle size and high QY. The results of this study provide a foundation for future biological applications, particularly for the development of *in vivo* optical stimulation applications.

Acknowledgments

This research was supported by a Grant-in-Aid for Scientific Research (A) (No. 22H00308: 2022–2025). Part of this study was supported by the Cooperative Research Project of the Research Center for Biomedical Engineering of the Ministry of Education, Culture, Sports, Science, and Technology of Japan.

References

1 T. Yanagida: J Ceram Soc Jpn. **133** (2025) 25064
2 T. Yanagida: Proc. Jpn. Acad., Ser. B **94** (2018) 75.
3 C. W. E. van Eijk: Phys. Med. Biol. **47** (2002) R85.
4 S. W. S. McKeever: Radiat. Meas. **46** (2011) 1337.
5 J. A. Rowlands: Phys Med Biol. **47** (2002) R123.
6 P. Leblans, D. Vandenbroucke, and P. Willems: Materials **4** (2011) 1034
7 N. Kawaguchi and T. Yanagida: Sens Mater. **31** (2019) 1257.
8 N. Kawaguchi, N. Kawano, G. Okada, and T. Yanagida: J. Lumin. **206** (2019) 634.
9 H. Masai, T. Yanagida, G. Okada, A. Koreeda, and T. Ohkubo: Sens. Mater. **29** (2017) 1391.
10 H. Kimura, T. Kato, D. Nakauchi, N. Kawaguchi, and T. Yanagida: J. Mater. Sci.-Mater. Electron. **30** (2019) 16755.
11 G. Okada, K. Shinozaki, D. Shiratori, N. Kawaguchi, and T. Yanagida: Ceram. Int. **45** (2019) 9376.
12 K. Asai, T. Ubukata, M. Koshimizu, Y. Fujimoto, T. Yanagida, and H. Kawamoto: J. Mater. Sci.-Mater. Electron. **30** (2019) 10211.
13 D. Shiratori, H. Kimura, Y. Fukuchi, and T. Yanagida: Sens. Mater. **36** (2024) 547.
14 D. Mouhssine, A. Nourreddine, A. Nachab, A. Pape, and F. Fernandez: Nucl. Instrum. Methods Phys. Res., Sect. B **227** (2005) 609.
15 G. M. Akselrod, M. S. Akselrod, E. R. Benton, and N. Yasuda: Nucl. Instrum. Methods Phys. Res., Sect. B **247** (2006) 295.
16 S. W. S. McKeever, S. Sholom, and N. Shrestha: Radiat. Meas. **123** (2019) 13.
17 H. Nanto: Sens. Mater. **30** (2018) 327.
18 E. Aşlar: Radiat. Meas. **154** (2022) 106779.
19 T. Kato, D. Nakauchi, N. Kawaguchi, and T. Yanagida: Opt. Mater. **132** (2022) 112785.
20 K. Ichiba, T. Kato, D. Nakauchi, N. Kawaguchi, and T. Yanagida: Sens. Mater. **36** (2024) 451.
21 T. Kunikata, P. Kantuptim, D. Shiratori, T. Kato, D. Nakauchi, N. Kawaguchi, and T. Yanagida: Sens. Mater. **36** (2024) 457.
22 S. Otake, H. Sakaguchi, Y. Yoshikawa, T. Kato, D. Nakauchi, N. Kawaguchi, and T. Yanagida: Sens. Mater. **36** (2024) 539.
23 N. Hayashi, and M. Koshimizu: J. Lumin. **277** (2025) 120993.
24 M. Koshimizu: Jpn. J. Appl. Phys. **62** (2023) 010503.
25 M. Koshimizu: J. Lumin. **278** (2025) 121008.
26 M. Hildebrandt, M. Koshimizu, Y. Asada, K. Fukumitsu, M. Ohkuma, N. Sang, T. Nakano, T. Kunikata, K. Okazaki, N. Kawaguchi, T. Yanagida, L. Lian, J. Zhang, and T. Yamashita: Int. J. Mol. Sci. **25** (2024) 11365.
27 S. Ding, H. Zhang, R. Dou, W. Liu, D. Sun, and Q. Zhang: J. Solid State Chem. **263** (2018) 123.
28 J. Chen, Y. Tang, X. Yi, Y. Tian, G. Ao, D. Hao, and S. Zhou: Opt. Mater. Express **9** (2019) 3333.
29 S. Li, Y. He, M. Li, F. Zeng, X. Wang, C. Sun, and Z. Su: J. Alloys Compd. **794** (2019) 227.
30 A. Nakanishi, T. Onoe, T. Maekawa, K. I. Murai and T. Moriga: J Lumin. **266** (2024) 120269.
31 Y. Luo, Z. Liu, H. T. Wong, L. Zhou, K.-L. Wong, K. K. Shiu, and P. A. Tanner: Adv. Sci. **6** (2019) 1900487.
32 A. Lempicki, A. J. Wojtowicz, and E. Berman: Nucl. Instrum. Methods Phys. Res., Sect. A **333** (1993) 304.
33 A. Sharma, M. Varshney, H. Saraswat, S. Chaudhary, J. Parkash, H. J. Shin, and S. O. Won: Int. Nano Lett. **10** (2020) 71.
34 R. D. Shannon: Acta A **32** (1976) 751.
35 M. Koshimizu, K. Tanahashi, Y. Fujimoto and K. Asai: Sens Mater. **37** (2025) 539
36 M. Koshimizu, Y. Fujimoto and K. Asai: Sens Mater. **35** (2023) 521.
37 I. R. Martín, F. Lahoz, V. Lavín and M. Hernández-Molina: Opt Mater. **25** (2004) 223.
38 K. Sawada and S. Adachi: J Lumin. **165** (2015) 138.
39 J. B. Gruber, U. V. Valiev, G. W. Burdick, S. A. Rakhimov, M. Pokhrel and D. K. Sardar: J Lumin. **131** (2011) 1945.
40 J. Bi, Q. Zhu, X. Li, J. Chen, X. Sun and J. G. Li: Mater Res Bull. **120** (2019) 110577.
41 X. Teng, J. Li, G. Duan and Z. Liu: J Lumin. **179** (2016) 165.
42 T. N. L. Tran, A. Chiasera, A. Lukowiak and M. Ferrari: Materials. **15** (2022) 1847.
43 I. Carrasco, F. Piccinelli and M. Bettinelli: J Lumin. **189** (2017) 71.
44 K. S. Sohn, Y. Y. Choi, K. H. Kim, S. Y. Choi and H. D. Park: J Mater Sci-Mater El. **12** (2001) 179.
45 G. Liu, X. Duan, H. Li, and D. Liang: Mater. Chem. Phys. **110** (2008) 206.